

Tracing the horizon of tetragonal-to-monoclinic distortion in pressurized trilayer nickelate $\text{La}_4\text{Ni}_3\text{O}_{10}$

Sitaram Ramakrishnan,^{1,*} Yingzheng Gao,^{1,†} Valerio Olevano,¹ Elise Pachoud,¹ Abdellali Hadj-Azzem,¹ Gaston Gabarino,² Olivier Perez,³ Alain Pautrat,³ Diego Valenti,¹ Matthieu Quénot,¹ Sébastien Pairis,¹ Dmitry Chernyshov,⁴ Leila Noohinejad,⁵ Carsten Paulmann,⁵ Sander van Smaalen,⁶ Pierre Toulemonde,¹ Marie-Aude Méasson,¹ and Pierre Rodière^{1,‡}

¹*Institut Néel CNRS/UGA UPR2940,*

25 Rue des Martyrs, 38042 Grenoble, France

²*ESRF – European Synchrotron Radiation Facility, 38000 Cedex Grenoble, France*

³*Laboratory CRISMAT, UMR 6508 CNRS,*

ENSICAEN 6 Boulevard du Marechal Juin, F-14050 Caen Cedex 4, France

⁴*Swiss-Norwegian Beamlines, ESRF – European Synchrotron*

Radiation Facility, 38000 Cedex Grenoble, France

⁵*Deutsches Elektronen-Synchrotron DESY,*

Notkestrasse 85, 22607 Hamburg, Germany

⁶*Laboratory of Crystallography, Bayerisches Geoinstitut,*

University of Bayreuth, 95440 Bayreuth, Germany

(Dated: December 5, 2025)

Abstract

The crux of understanding the superconducting mechanism in pressurized Ruddlesden–Popper nickelates hinges on elucidating their structural phases. Under ambient conditions, the trilayer nickelate $\text{La}_4\text{Ni}_3\text{O}_{10}$ stabilizes in a twinned monoclinic structure with space group $P2_1/c$. Upon heating, it undergoes a structural transition to the tetragonal $I4/mmm$ phase at $T_s \approx 1030$ K, while a second transition associated with the onset of density-wave (DW) ordering emerges upon cooling below $T_{DW} \approx 135$ K. Here, from pressure-temperature x-ray diffraction on high quality flux-grown single crystals we unequivocally demonstrate a direct tetragonal-to-monoclinic transition with no trace of an intermediate orthorhombic $Bmab$ phase. *Ab initio* density-functional theory calculations as a function of pressure fully corroborate the experimental observations. The transition unfolds as a 2-fold superstructure due to the emergence of commensurate superlattice reflections and can be progressively suppressed from 1030 K down to 20 K under 14 GPa. No discernible structural distortions associated with DW ordering are detected down to 20 K at ambient pressure. This in contrast to Raman measurements that reveal the appearance of additional phonon modes below 130 K, implying a further reduction in symmetry from monoclinic $P2_1/c$ and thus indicating the presence of a third structural phase associated with the DW ordering in $\text{La}_4\text{Ni}_3\text{O}_{10}$.

Groundbreaking scientific discoveries in Cu-based superconductors, where the superconductivity (SC) is believed to arise from the partially filled Cu $3d$ electron states in the CuO_2 planes have fundamentally shaped our understanding of high temperature SC over the years [1–3]. Nevertheless, the microscopic mechanisms underlying their unconventional superconductivity remain an enigma. In this context, the search for analogous materials continues to be of paramount importance. Rare-earth nickelates have emerged as a fertile platform for exploring correlated electron phenomena. Like the cuprates, they host a rich interplay of quantum phases including charge and spin density waves, antiferromagnetism, and superconductivity offering new avenues to probe the intertwined nature of these competing orders [4–8].

Experimental evidence of SC in the nickelates was first realized on thin films of infinite-layer $\text{Nd}_{1-x}\text{Sr}_x\text{NiO}_2$ [9–11]. Interestingly, this structure, composed of NiO_2 planes stacked along the c axis, hosts Ni^{1+} ions with a $3d^9$ electronic configuration, formally isoelectronic

* niranj002@gmail.com; Equal contribution

† Equal contribution

‡ pierre.rodier@neel.cnrs.fr

to Cu^{2+} in the cuprates. However, superconductivity has not been observed in bulk crystals [12], suggesting a notable influence of the substrate. This breakthrough was shortly followed by the discovery of high temperature SC at $T_c = 80$ K under hydrostatic pressure in bulk Ruddlesden-Popper bilayer crystal of $\text{La}_3\text{Ni}_2\text{O}_7$, where the average electronic structure of the Ni is $\text{Ni}^{2.5+}$ ($d^{7.5}$) far from the analogs to the cuprates. Interestingly, the SC is accompanied by a change in the symmetry of the crystal structure [13–18].

Recently, SC up to 30 K was also discovered both in bulk Ruddlesden-Popper trilayer crystals $\text{La}_4\text{Ni}_3\text{O}_{10}$ and $\text{Pr}_4\text{Ni}_3\text{O}_{10}$ [19–22]. The emergence of superconductivity was evidenced by a drop in the electrical resistance and an anomaly in the magnetic susceptibility around $P_c \approx 15$ GPa. Notably, the reported critical pressure spans a broader range of 5–40 GPa depending on the transmitting medium and the criteria chosen to define the T_c [19]. Both compounds at room temperature undergo a change in symmetry from monoclinic $P2_1/c$ to tetragonal $I4/mmm$ at $P_c \approx 15$ GPa [19–22], where at ambient pressure the transition towards monoclinic symmetry occurs at $T_S \approx 1030$ K for $\text{La}_4\text{Ni}_3\text{O}_{10}$ [23, 24]. This suggests that SC emerges once the material has been restored to the higher tetragonal symmetry phase. In addition under ambient pressure, a density wave (DW) ordering associated with spin and charge manifests in $\text{La}_4\text{Ni}_3\text{O}_{10}$ at $T_{DW} \approx 130$ K, characterized by the emergence of incommensurate modulation observed in single crystal by x-ray and neutron diffraction [25], followed by other probes [26, 27]. This DW ordering marked by an anomaly in resistivity and magnetic susceptibility measurements is remarkably fragile as it collapses under the application of a few GPa [19, 28], which presumably is the trigger to promote spin fluctuations. This can be attributed to a pairing mechanism for the formation of the Cooper pairs [29–34]. However, the pressure-dependence of T_{DW} remains enigmatic as optical spectroscopy experiments do not corroborate the transport measurements, thereby stating that the DW competes with the SC [35]. Studies involving temperature dependent powder x-ray diffraction (PXRD) on $\text{La}_4\text{Ni}_3\text{O}_{10}$ reveals a negative thermal expansion of the b axis that could be potentially linked to structural distortions associated with density-wave ordering [36–38]. However, the symmetry in the incommensurate phase and the extent to which it can reshape the 3-dimensional (3- d) lattice remains shrouded in uncertainty as later works do not reproduce or probe the modulation through x-ray diffraction.

Further analysis regarding the modulation is prefaced by a lingering matter pertaining to the symmetry of $\text{La}_4\text{Ni}_3\text{O}_{10}$ at ambient conditions, as it also remains in a state of quandary.

Some reports identify single crystals as orthorhombic $Bmab$ rather than monoclinic $P2_1/c$ symmetry [37]. A follow up work by Li et al., [22] propose an experimental phase diagram based on x-ray and transport measurements on single-crystalline $\text{La}_4\text{Ni}_3\text{O}_{10-\delta}$. However, it is not yet elucidated from a crystallographic point of view. Careful investigation of the diffraction pattern at 11 GPa revealed extremely weak reflections that appear to violate the B -centering, an observation that can be ascribed to the formation of twin domains resulting from symmetry breaking, closely resembling our diffraction pattern. However, their interpretation differs from our present work.

In this paper, we seek to resolve the persistent ambiguities surrounding the symmetries reported in this material by constructing a unified crystallographic framework that connects the disparate phases. Our crystallographic analysis unveils a direct transition from tetragonal ($4/mmm$) to monoclinic ($2/m$), with the latter emerging as a 2-fold superstructure of the former. This is further reinforced by *ab initio* density-functional theory (DFT) calculations which also unequivocally demonstrates the absence of any intermediate phase between the monoclinic and the tetragonal $I4/mmm$. The absence of an orthorhombic $Bmab$ phase evidenced by minute deviations of the monoclinic angle from 90° and improved fit to the XRD data employing $P2_1/c$ symmetry suggests that superconductivity emerges within the tetragonal symmetry under pressure, consistent with previous reports [19, 20, 22]. We further track the evolution of the structural transition temperature T_S under hydrostatic pressure, observing a reduction from 1030 K at ambient conditions to 20 K under hydrostatic pressures of 14 GPa. Lastly, while XRD under ambient pressure detects no incommensurate satellites associated with density-wave ordering down to 20 K, Raman scattering on the other hand reveals emergence of additional phonon modes ≈ 130 K. This is indicative of subtle lattice distortions induced by the DW ordering that ultimately renders the structure to be below $2/m$ symmetry.

RESULTS AND DISCUSSION

High-temperature powder X-ray diffraction (PXRD) measurements under ambient pressure carried out at beamline BM01 of ESRF in Grenoble, reveal a structural transition from the tetragonal to the monoclinic phase at $T_S \approx 1030$ K, in close agreement with [23, 24]. As in previous studies [25, 36] the minute lattice distortion manifested as a small deviation of

β from 90° by $\approx 0.1\text{--}0.2^\circ$ as shown in Figure S1 in the supporting information (SI) [39] can only be understood by employing non-standard crystallographic settings. However, earlier works do not explicitly describe the transformations between standard monoclinic $P2_1/c$ to non-standard $B2_1/a$ and standard tetragonal $I4/mmm$ to non-standard $F4/mmm$, thereby inadvertently obscuring symmetry relationships. Presently, we have discussed the transformations (See supporting information (SI) [39] and Figure 3) to emphasize the importance of maintaining a consistent crystallographic framework in view of connecting both phases and to avoid the misleading impression of a large monoclinic distortion that arises in the standard setting $P2_1/c$ with $\beta \approx 100^\circ$, thus enabling a more transparent and meaningful description of how the distortion evolves under temperature and pressure. To map the evolution of this structural transition by pressure, single-crystal X-ray diffraction (SXRD) under pressure was performed at the beamline ID15b of the ESRF. Application of hydrostatic pressure suppresses the transition, as elucidated by the phase diagram shown in Figure 1, which reveals a pronounced reduction of the transition temperature to 20 K under an applied pressure of 14 GPa.

Establishing the critical pressure and temperature points for the phase diagram required rigorous scrutiny of reflections in the $hk0$ plane as shown in Fig. 2. The reflections, nearly circular in the high-pressure tetragonal phase, become progressively broadened and anisotropic as the transition sets in, eventually splitting into distinct components at lower pressures. This bifurcation of the reflections becomes particularly pronounced at low temperatures 80 and 20 K, stating that the evolution of the distortion in the structure is significantly tuned by both pressure and temperature. Furthermore, we state the emergence of the monoclinic ($2/m$) phase in $\text{La}_4\text{Ni}_3\text{O}_{10}$ defies interpretation as a mere distortion of the tetragonal lattice. As illustrated in Figure 2 (b) upon indexing the diffraction maxima on the high-pressure I -centered 'pseudo-tetragonal' lattice ($a = b \approx 3.7 \text{ \AA}$, $c \approx 27 \text{ \AA}$) reveal that the onset of the $2/m$ phase is marked by superlattice reflections at commensurate positions $\mathbf{q}^1 = (\frac{1}{2}, \frac{1}{2}, 0)$ and $\mathbf{q}^2 = (\frac{1}{2}, -\frac{1}{2}, 0)$ along with mixed-order satellite reflections corresponding to linear combinations of \mathbf{q}^1 and \mathbf{q}^2 . Rather than invoking higher-dimensional ($3 + n - \text{dimensional}$) superspace formalism [40], where the intensities of the main Bragg reflections are kept distinct from the superlattice peaks, we reproduce the solution of the monoclinic structure in 3-dimensions by indexing and integrating as a superstructure, echoing earlier works [19, 20, 22, 24, 25]. The resulting monoclinic structure is effectively 2-fold relative to the parent tetragonal phase,

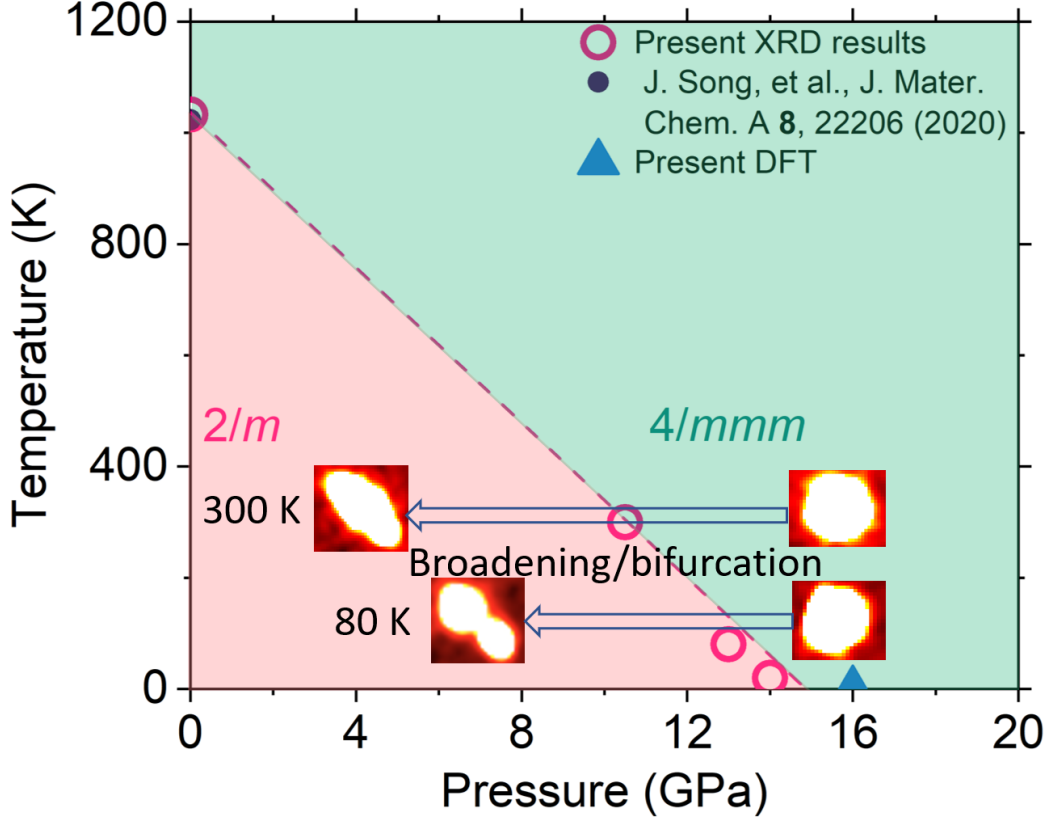


FIG. 1. Pressure-temperature phase diagram illustrating the tetragonal-to-monoclinic structural transition. Dashed line serving as a visual guide to indicate the linear suppression and signifies the phase boundary between $4/mmm$ and $2/m$ symmetries. The present result of XRD above 1000 K closely matches the work done in the past [23, 24]. Our complementary *ab-initio* calculations predict a critical pressure point $P_c \approx 16$ GPa at 0 K, in good agreement with experimental observations, thereby reinforcing its validity. Bragg reflections at room temperature and at 80 K are also shown to illustrate their evolution from $4/mmm$ to $2/m$. Upon entering the monoclinic phase they tend to broaden and become anisotropic.

as the $P2_1/c$ unit cell corresponds to twice the volume of the primitive triclinic cell derived from the $I4/mmm$ lattice.

From Figure 2 (c) showing panels where the lattice has been indexed as $a \approx 5.41$ Å, $b \approx 5.43$ Å, $c \approx 27$ Å (LP-non-standard setting) indicates the presence of new reflections that appear to violate centerings at lower pressure points. However, it manifests from the microscopic domains of the single crystal induced by the phase transition, similar to the more recent work by Li, et al., [22]. Figure 3 (c) shows the deviation of the Ni1-O2-Ni2 bond

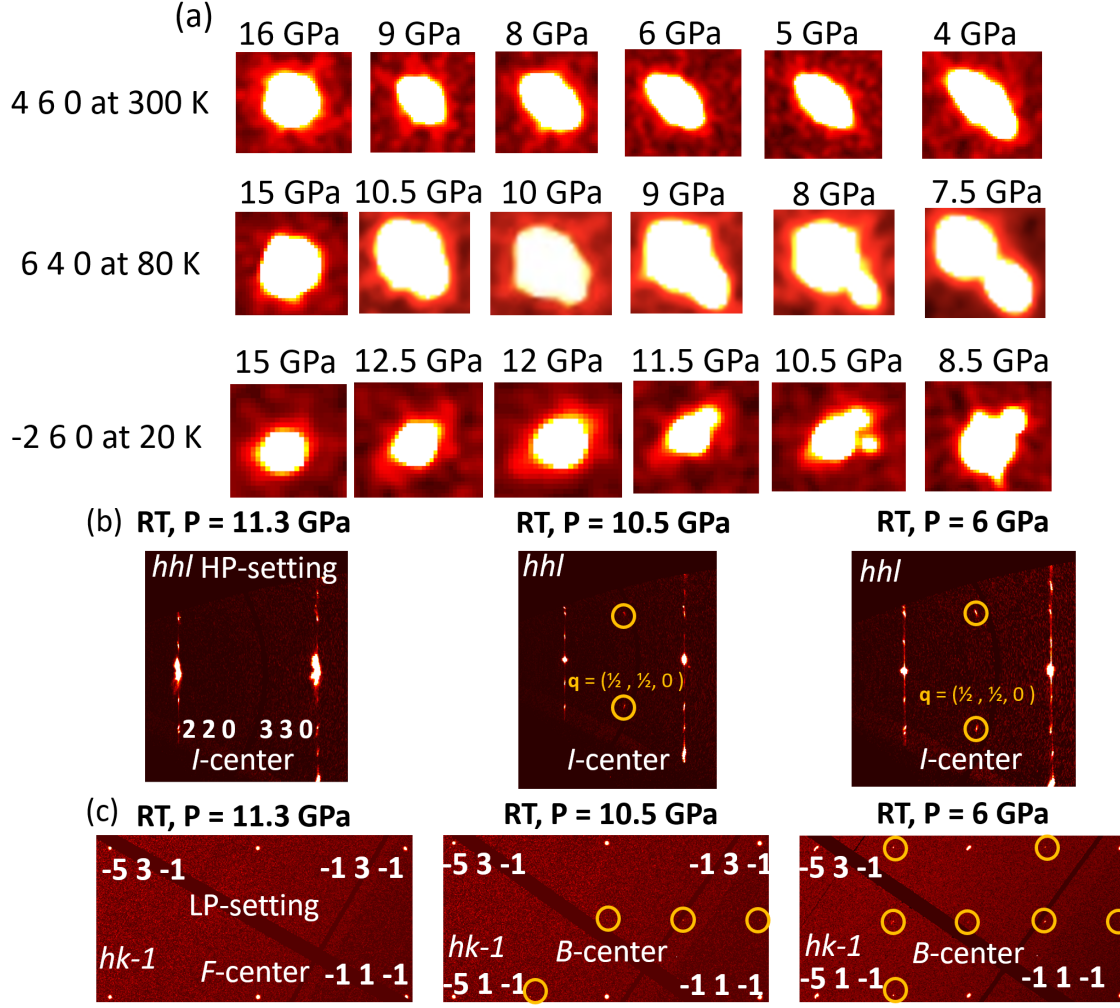


FIG. 2. (a). Reconstructed reciprocal layer showing specific reflections indexed in non-standard settings in the $hk0$ plane at 300, 80 and 20 K. At on the onset of the structural transition from $4/mmm$ to $2/m$, the reflection becomes broader and stretched and later splitting into two at lower temperatures 80 and 20 K, indicative of pseudo-merohedral twinning resulting from the monoclinic distortion of the lattice. (b). Excerpts of the hhl plane where yellow circles indicate superlattice reflections at $\mathbf{q} = (\frac{1}{2}, \frac{1}{2}, 0)$ when indexed on the HP (High Pressure) standard-lattice that corresponds to an I -centered pseudo-tetragonal lattice where $a = b \approx 3.7$ Å, $c \approx 27$ Å. (c) Panels of the reciprocal layers of the $hk-1$ plane of the LP (Low Pressure) non-standard-lattice where $a \approx 5.41$ Å, $b \approx 5.43$ Å, $c \approx 27$ Å and $\beta \neq 90^\circ$, showing presence of twinning due to weak diffraction spots indicated by yellow circles below 11.3 GPa. The lattice is $F4/mmm$ at 11.3 GPa and below that it reduces to $B2_1/a$.

angle from 180° that corresponds to the tilt of the NiO_6 octahedra along \mathbf{c} upon entering the $2/m$ phase, thereby highlighting the effect of the phase transition on an atomic level. Figure 3 also illustrates that $\text{La}_4\text{Ni}_3\text{O}_{10}$ consists of three layers of Ni planes, with each Ni atom surrounded by six oxygen to form an octahedral site. The inner layer is sandwiched between two outer layers. The outer layers of different blocks are stacked with a rock salt layer of LaO. It is worth noting that the octahedral sites are strongly distorted. Each Ni atom in the inner layer has two apical oxygen (i.e. along the c -axis in the pseudo-tetragonal description of the structure), which are close together, and four oxygen in the basal plane, which are further apart. The octahedra in the outer layers differ. Indeed, the apical O close to the rock salt layer (O_4) and the four O in the basal plane (O_3) form a square-based pyramid, and the second apical O (O_2) shared with the inner layer Ni is far away. At 15 GPa, the octahedra is perfect. As it was already noticed by the previous work, at low pressure, the NiO_6 blocks are tilted from the pseudo c -axis.

Evolution of the lattice parameters can be inferred from Figure 4(a)–(b) the distortion toward monoclinic symmetry is minimal, particularly at 300 K where it is negligible. Much like the structural transition at ambient pressure outlined in the SI [39] in Figure S1, it is also noted that in Figure 4 (b) there is a jump in the value of β at the onset of the $2/m$ phase, which could be attributed to a weak first-order phase transition. The loss of symmetry from $4/mmm$ to $2/m$ generates four twin domains whose relation is explained in the SI [39]. Essentially, these domains are described by distinct twin laws, and their presence is evident from reflection splitting in the diffraction data as shown in Fig. 2. The degree of overlap between the domains referred to as the ‘twin obliquity’ is partial and indicates pseudo-merohedral twinning as observed from Figure 2. Detailed information pertaining to the concept of twinning by phase transformation can be obtained from Parsons [41]. The splitting appears to increase at 80 and 20 K, which contributes to the increase the distortion of the lattice computed by $(b - a)/(b + a)$ at lower temperatures as depicted in Figure 4(c). Lattice parameters and Volume as inferred from 4(d) decreases monotonously with increasing pressure and the equation of state (EOS) fit depicting its compressibility is in good agreement with [19]. Details of the EOS fit are given in the SI [39]. Recent work by Li, et al., [22] suggests the presence of an intermediate phase where the symmetry is $Bmab$ which is in contrast to what we propose, as the transition from $4/mmm$ to $2/m$ is continuous bypassing the orthorhombic phase due to the lack of orthogonality of β as observed from

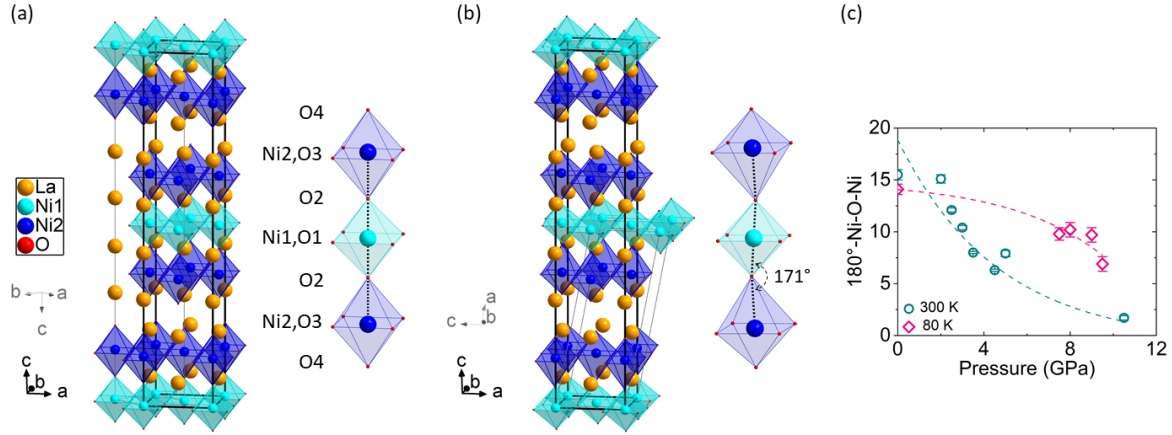


FIG. 3. Crystal structures of $\text{La}_4\text{Ni}_3\text{O}_{10}$. (a) The high pressure phase (15 GPa) at room temperature where the crystal structure is tetragonal. The $F4/mmm$ structure whose unit cell indicated by thick lines is superimposed onto the standard $I4/mmm$ structure to have a visual representation of the transformation between the two, where bond angle of Ni1-O2-Ni2 is 180° . (b) Monoclinic phase at room temperature 6 GPa. Here the $B2_1/a$ structure (thick lines) has been drawn onto the standard $P2_1/c$ structure (thin lines) to show the transformation between the two visually, where bond angle of Ni1-O2-Ni2 is 171.1° . The mathematics of the transformations are described in the SI [39]. (c) Evolution of the octahedral tilt as a function of pressure at 300 and 80 K. Dashed lines are just a guide to the eye.

pressure-temperature dependent XRD measurements. Although β is close to 90° (See Fig 4 (b)) at room temperature under pressures of 10.5 GPa which is the onset of the transition, the fit to the data employing monoclinic symmetry $B2_1/a$ compared to orthorhombic $Bmab$ is much better as shown in Table S4 in the SI [39]. Tiny deviation of the axial angles from 90° is not uncommon and develops in other materials like CDW compound SrAl_4 [42], incommensurately modulated Rb_2ZnCl_4 [43], antiferromagnetic Eu_2Sb_3 [44], incommensurate phase of ferroelectric KNbO_3 [45] and the superstructure phase of CoSn_2 [46]. Table S5 in the SI [39] shows the crystallographic information and the lattice parameters indicate the monoclinic distortion is rather minute, thus the lattice is pseudo-tetragonal. Atomic coordinates are also listed in the SI [39].

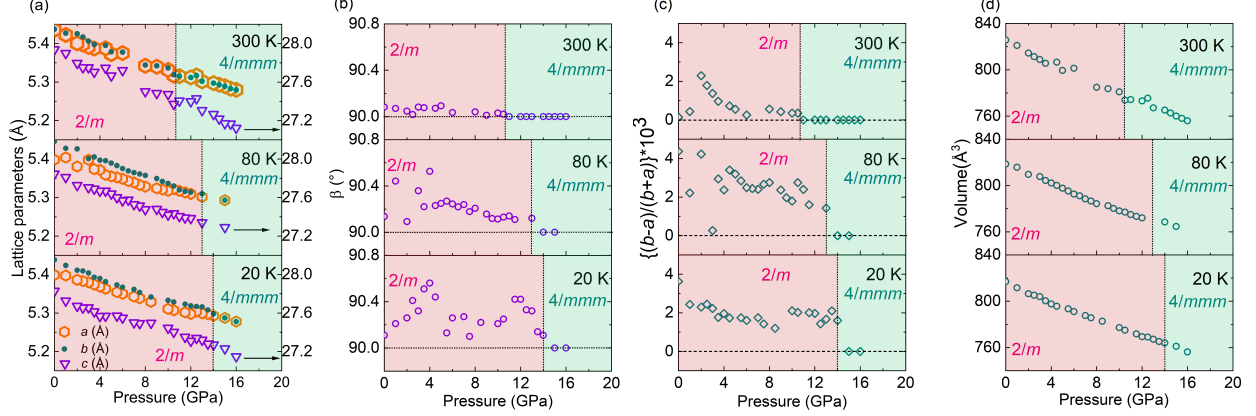


FIG. 4. (a)–(d) Lattice parameters, distortion and the volume within the pressure range of 0–16 GPa for temperatures at 300, 80 and 20 K. In the tetragonal phase ($4/mmm$), the lattice parameters correspond to the non-standard F -centered setting of $I4/mmm$ and for the monoclinic phase ($2/m$) we use the $B2_1/a$ non-standard space group in order to preserve the same setting of the lattice which allows for a comparison. Error bars are smaller than the symbols which can be understood from the numerical values listed in Table S5 in the SI [39]. Fits of a Birch-Murnaghan equation of state (EOS) to the volume-pressure data has resulted in $V_0 = 825(1) \text{ \AA}^3$ and $K_0 = 155(4) \text{ GPa}$ at 300 K, $V_0 = 818(1) \text{ \AA}^3$ and $K_0 = 182(4) \text{ GPa}$ at 80 K, and $V_0 = 815(1) \text{ \AA}^3$ and $K_0 = 185(2) \text{ GPa}$ at 20 K. See the SI for details [39].

The subtlety of the direct tetragonal-to-monoclinic phase transition realized from XRD can also be understood from Fig. 5, where we present the results of an *ab initio* density-functional theory (DFT) crystal structure relaxation using the PBE [47] generalized-gradient approximation (GGA). The calculations at all pressures have been carried out within the least symmetric monoclinic spacegroup 14 in the $P2_1/c$ setting, which is a subgroup of both the orthorhombic $Bmab$ and the tetragonal $I4/mmm$, namely $P2_1/c \subset Bmab \subset Fmmm \subset I4/mmm$. Therefore, our crystal relaxation is free to span all these four structures and can address all the transitions between these four phases. The figure presents the evolution with pressure of the three order parameters associated to these transitions, namely: the orthorhombic distortion factor o taken as the basal distortion $o = (b - a)/(a + b)$, associated to the orthorhombic-tetragonal $Fmmm \rightarrow I4/mmm$ phase transition; the NiO octahedra tilt angle $\theta = 180 - \text{Ni1-O2-Ni2}$ between the two Ni and the O apical atom, associated to the $Bmab \rightarrow Fmmm$ phase transition; the “monoclinicity” (monoclinic distortion) angle

$\beta - 90$ degrees, associated to the monoclinic-orthorhombic $P2_1/c \rightarrow Bmab$ phase transition. β is the angle between the **a** and **c** vectors of the primitive cell in the $B2_1/a$ setting, read after having applied the $P2_1/c \rightarrow B2_1/a$ transformation matrix, in close analogy to the experimental analysis presented earlier.

The figure shows unequivocally that, for *ab initio* DFT PBE, the system undergoes only one phase transition, from the monoclinic $P2_1/c$ directly to the tetragonal $I4/mmm$. *There is no room for intermediate structures*: both the orthorhombic $Bmab$ found by Ref. [22], and also a hypothetical orthorhombic $Fmmm$ without octahedra distortions, are definitely ruled out. Indeed, the three order parameters all nullify at the same critical pressure found to be $P_c = 16.47 \pm 0.04$ GPa. The error refers just only to the spread between the three independent P_c obtained by a fit on the three order parameters, and does not include the error associated to the PBE approximation.

It is well known that the PBE approximation overestimates lattice parameters by at least 1%, and the error increases for example on the c parameter of layered hexagonal crystals. At $T = 0$ K and $P = 0$ GPa our DFT PBE relaxation provided $a = 5.43$ Å, $b = 5.51$ Å, and (in the $B2_1/a$ setting) $c = 27.89$ Å with $\beta = 90.42$ deg, and finally $\theta = 17.25$ deg. With respect to the experiment at $T = 20$ K, $P = 0$ GPa, we see that here the PBE overestimation is slightly below 1% on a , slightly above 1% on b , and remarkably only 0.3% on c . There is no common consensus on the PBE error on lattice angle parameters. Here we see that PBE and XRD at least agree on the order of magnitude. It can be expected that the systematic overestimation on lattice parameters leads also to overestimation of critical pressures. If we estimate the error on pressure as the value here required to shrink the b parameter by 1%, we will get $\Delta P = 3$ GPa. This is the most pessimistic estimate, but we cannot be more optimistic than $\Delta P = 1$ GPa. In any case, if the quantitative result on P_c might be affected by a large PBE error, the qualitative result on the non-existence of intermediate phases, is much less questionable.

In Fig. 5 we also show by dashed lines our best fits on the three last points closest to the critical pressure. We have used a standard scaling $\sim (P_c - P)^\alpha$ with $\alpha = 1/2$ both for the octahedra tilt angle θ and for the monoclinic β angle, while a linear fit has been used for the basal distortion $b - a$. The square-root scaling is closely respected by the θ parameter down to $P = 0$. The θ scaling and magnitude seems in agreement with the experiment (see Fig. 3c at 80 K). On the other hand, we observe a quick breakdown for the monoclinic β parameter.

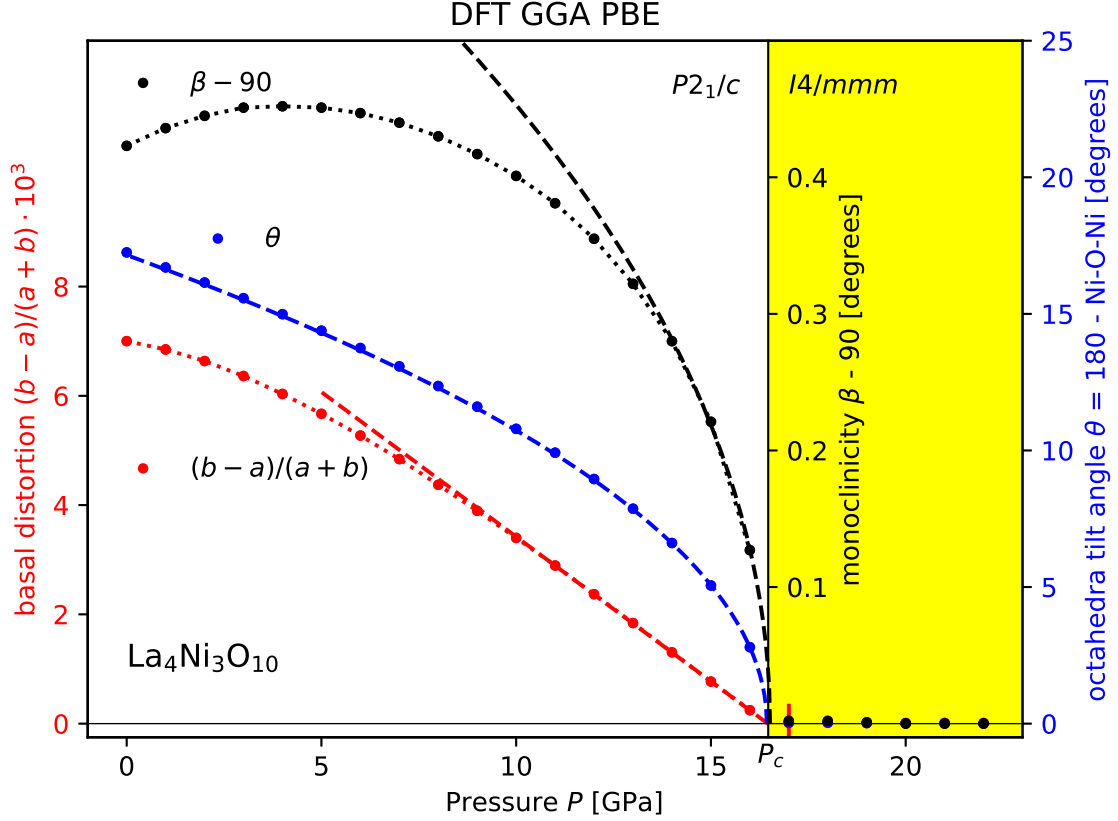


FIG. 5. Density-functional theory GGA PBE crystal relaxation as a function of applied external pressure: red dots and lines: basal distortion $(b-a)/(a+b)$ to be scaled by 10^3 (red leftmost y axis); blue dots and lines: NiO octahedra tilt angle $\theta = 180 - \text{Ni1-O2-Ni2}$ in degrees (blue rightmost y axis); monoclinic angle $\beta - 90$ in degrees (black middle y axis placed at P_c). Both horizontal and vertical error bars are smaller than the dot size when not visible. Dashed lines refer to fits, whereas dotted lines are just only a guide to the eyes.

Letting the critical coefficient free in the fit provides $\alpha = 0.4$ but without any improvement on the low pressure side. Remarkably, the monoclinic angle β presents a maximum at ~ 4 GPa signaling a departure from a simpler mean-field description. It would be interesting to check the existence of such maximum in XRD data, but the lowest level of monoclinicity $\beta \sim 10^{-1}$ deg close to the experimental accuracy, will make it difficult. Finally, we also remark that the basal distortion σ is linear down to 9 GPa, and then we observe a departure from linearity again in the region where the system presents its maximum monoclinicity.

On the other hand, our *ab initio* DFT PBE calculation of the crystal structure carried

within the $P2_1/c$ elementary cell cannot state anything about the possibility of a density wave (DW). We could in principle check the possibility of a *commensurate* DW by carrying the calculation within the supercell at the corresponding superperiodicity, but this is impossible in the case of an *incommensurate* DW.

Despite extensive temperature-dependent high-pressure SXRD measurements down to 20 K, no signatures of incommensurate modulation associated with density wave (DW) ordering were detected, contrary to what was observed by Zhang et al. [25]. To eliminate the possibility that weak satellite reflections were obscured by background scattering from the diamond anvil cell or residual pressure effects, we conducted low-temperature SXRD experiments under ambient-pressure at P24 beamline DESY, Hamburg using the same batch of single-crystals. These measurements below 130 K likewise revealed no incommensurate satellites in any region of reciprocal space as shown in Figure S4 in the SI [39], thereby suggesting the weak nature of any incommensurate modulation. Crystallographic data for the data collected in DESY are provided in the SI [39].

Notably, Zhang et al.’s [25] study provided limited quantitative analysis of the lattice modulation, and later investigations have not reproduced the reported low-temperature single-crystal XRD results. The lack of discussion surrounding the results possibly stems from a multitude of problems such as the weak intensity of the incommensurate satellites or its manifestation due differences in crystal growth strategies, which presumably plays a decisive role in stabilizing the structural transitions in $\text{La}_4\text{Ni}_3\text{O}_{10}$. However, Raman spectroscopy proved to be successful to verify the distortion thanks to the emergence of new phonon modes in the DW phase.

In the space group $P2_1/c$ (no. 14, standard setting), at room temperature, the Wyckoff positions are identified to be $8\ 4e$ and $1\ 2a$ (Ni atoms). Thus, the number of phonon modes is expected to be: $\Gamma=24A_g+24B_g+27A_u+27B_u$. The Raman-active phonons are $24\ A_g$ and $24\ B_g$, which are active in parallel and crossed polarizations, respectively, when the Poynting vector is perpendicular to the (bc) plane (here we use the standard setting with b as unique axis, Cf. Fig. 3). The Raman activity is reported in table I. All these modes have single degeneracy. As shown Fig. 6.a, 15 modes in parallel and 19 in crossed polarization configurations are identified by polarized Raman spectroscopy at 170 K (so above the transition temperature), consistent with the reported space group $P2_1/c$. New modes appear at low temperature between 120 K and 150 K, as show Fig. 6.c and d. At

26 K (Cf. Fig. 6.b), 31 modes in parallel configuration and 20 ones in crossed polarization configurations are measured. This evaluation of the number of modes appearing at low temperature has been done in a conservative way (Cf. SI), so these are minimum numbers of modes. The number of modes in parallel polarization as well as the total number of modes exceeds the authorized ones in the $P2_1/c$ room temperature space group. Thus we can conclude safely to a lowering of symmetry below ~ 120 K. We will come back to this change of symmetry later on. Recent reported results by Gim *et al.* [48] presented the phonon modes up to 120 meV ($=970\text{ cm}^{-1}$). They do not report any new mode at low temperature whereas we observe many new ones in this energy range. Other recent publications [49, 50] reported the appearance of new modes at low temperature. Interestingly, Suthar *et al.* observed a total of 48 modes at low temperature (24 in each polarization configurations), so it is still consistent with the room temperature space group. Our results, while being quite similar in many aspects (behavior of peculiar phonons, energies of phonon modes), show more than 48 modes at low temperature, thus ruling out the $P2_1/c$ as the low temperature space group. In the SI [39], we report a full list of our detected phonon modes. Generally, the samples' quality and exact composition seems to have important impact on the Raman responses, pointing to this characterization technique as a sensible one.

Some modes, already measured at room temperature, exhibit peculiar behaviors with decreasing temperature and particularly concomitantly with the appearance of new modes, i.e. at about T_{DW} . As presented Fig. 6(e), the A_g mode at about 350 cm^{-1} (red triangle) softens, loses intensity and gets broader at low temperature, all unexpected phonon behaviors. The A_g mode at about 470 cm^{-1} (blue triangle) exhibits an upturn in its hardening while demonstrating a clear broadening at a similar temperature of ~ 120 K. Reminding that no splitting is expected from these single degenerate modes, a change of electron-phonon coupling through the transition most probably explains such behaviors. We note that the new mode at 515 cm^{-1} becomes narrower when cooling down, contrary to what was reported by Suthar *et al.* [49]. Finally, other broad features above 600 cm^{-1} , already present at 300 K, are detected in the electronic Raman response. We discuss them in the S.I [39].

The new modes appearing below ~ 120 K are interpreted as phonons, naturally originating from a transition, either a purely structural distortion or alternatively an electronic one

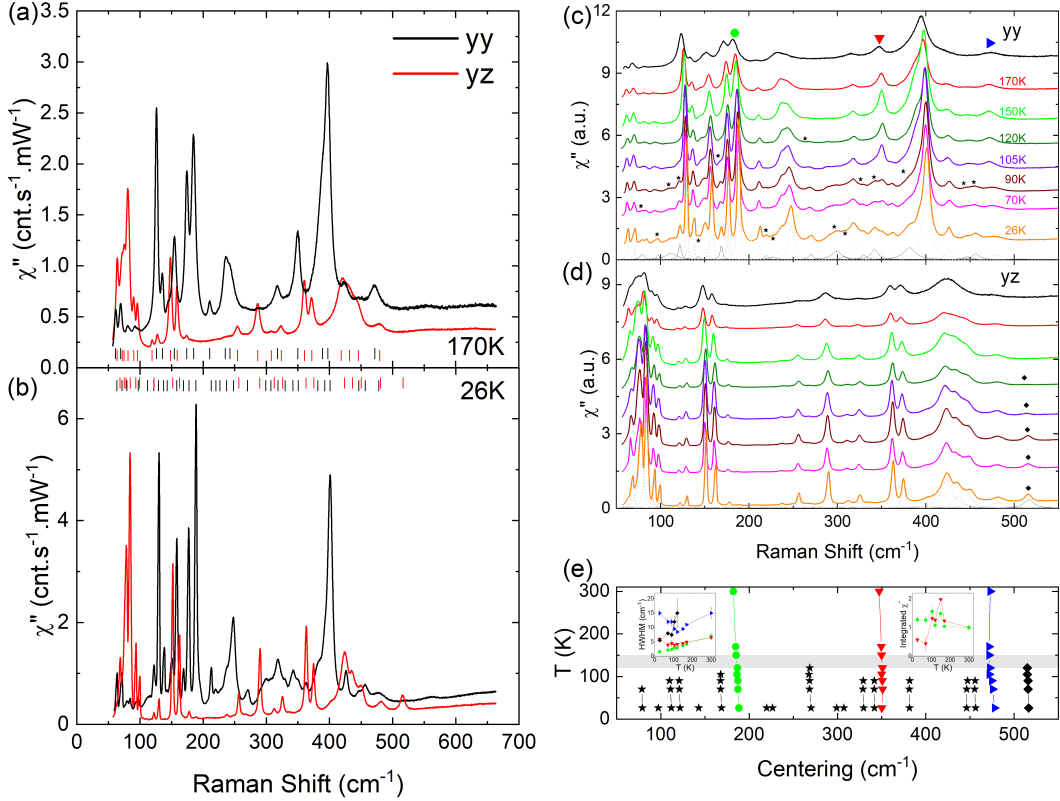


FIG. 6. Raman spectra of $\text{La}_4\text{Ni}_3\text{O}_{10}$ with polarizations in the (bc) plane (standard setting) and in both yy and yz configurations, at 170 K (a) and 26 K (b). Clearly identified phonons are reported as ticks (red : yz , black: yy). (c)-(d) Spectra as a function of temperature in yy (c) and yz (d) configurations of polarizations of light. The modes that emerge across the transition at ~ 130 K are highlighted with diamond (yz) and stars (yy). Their fits at 26 K are shown by plain black lines. The modes that strongly change with temperature are shown with triangles. The green dot mode is a common-behavior phonon modes for comparison. (e) Phonon energy as a function of temperatures for the new modes and the modes with peculiar behaviors. The grey region indicates the transition temperature range. Insets: (on the left) Half-width-at-half-maxima (HWHM) and (on the right) integrated susceptibilities normalized at 300 K of the selected modes.

which backfolds the phonon modes originally at finite \vec{Q} into Γ point of the Brillouin zone. Structural transition is puzzlingly not observed by our XRD measurements at ambient pressure and low temperature, whereas samples are synthesized with the same technique. We discuss here the possible structural transitions, starting from the sub-groups of the Room

temperature space group, i.e. $P\bar{1}$, Pc , $P2_1$ and $P1$. The $P\bar{1}$ group with 16 $2i$, 1 $1a$ and 1 $1e$ occupied Wyckoff positions would allow 48 A_g modes, active in both parallel and crossed polarization configurations. Since we measure a total of 51 phonon modes at low temperature, we can certainly rule out $P\bar{1}$ as the low temperature space group. Pc and $P2_1$ sub-groups both non-centrosymmetric, allow the initially IR active mode to become Raman active. With 17 $2a$ occupied Wyckoff positions, we then expect 51 A (A') and 51 B (A'') modes for $P2_1$ (Pc) group. These large numbers of active phonon modes is then compatible with our observations by Raman spectroscopy. Beside each mode clearly follows the Raman selection rules (crossed versus parallel polarizations) as expected for these duo of symmetries (A/B or A'/A'').

Although Raman spectroscopy is not the most incisive probe for deciphering the symmetry of the structure, our measurements nevertheless suggest a breaking of $2/m$ symmetry below 130 K. Yet there is an intriguing twist, since Raman scattering is not fully tailored to analyze incommensurate structures. The emergence of a modulated state breaks translational symmetry, causing the familiar Raman selection rules to be no longer applicable. As a result, any assignment of the symmetry drawn from the present data must ultimately be revisited once a credible superstructure approximation is established, ideally through resolving the symmetry of the incommensurate phase employing the superspace approach [40]. From XRD we note that the average structure (three-dimensional (3- d) lattice) is nominally monoclinic, the incommensurability tends to transcend this simple description as it apparently drives a further reduction in symmetry. However, for our case the incommensurate satellite reflections are too weak and remain undetected down to 20 K at ambient pressure, thereby preventing a quantitative assessment of this symmetry lowering. Such cases where the modulation plays a decisive role in breaking of symmetry, while the 3- d lattice shows no distortion is ubiquitous in many incommensurate systems like Mo_2S_3 , CuV_2S_4 , EuAl_4 , SrAl_4 , $\text{Sm}_2\text{Ru}_3\text{Ge}_5$ and $\text{Gd}_2\text{Os}_3\text{Si}_5$ [42, 43, 51–55].

To conclude, we state that the monoclinic phase consistently manifests as a twinned two-fold superstructure below 1030 K which is easily observed by XRD. This behavior implies that under ambient conditions the crystal inherently accommodates four crystallographically oriented twins and that the transition from tetragonal-to-monoclinic symmetry is remarkably impervious to variations in the crystal growth process, whether it be by flux or the floating zone method. The monoclinic distortion is exceedingly minimal, thereby maintain-

ing an overall pseudo-tetragonal crystallographic framework. Pressurizing the material from ambient conditions to 14 GPa leads to a gradual suppression of the distortion over a broad temperature range from 1030 K to 20 K, reflecting its delicate energetic balance. Guided by *ab initio* calculations and pressure-temperature dependent XRD measurements, we state that the tetragonal-to-monoclinic phase transition is subtle and direct, devoid of an intermediate orthorhombic *Bmab* phase. By adopting a consistent crystallographic description, we are able to elucidate how the symmetries of the two phases evolve and are interconnected, thereby resolving the long-standing ambiguities among the tetragonal, orthorhombic and monoclinic structures. This affirms that superconductivity emerges only once the system is restored to the tetragonal phase under pressure.

The periodic lattice distortion associated with DW ordering below 130 K remains elusive, as it remains below the detection threshold of our XRD experiments employing synchrotron radiation. Low-temperature single-crystal XRD measurements reveal no incommensurate satellite reflections below 130 K, preventing a quantitative description of the modulation. Nevertheless, Raman spectroscopy detects additional vibrational modes. The emergence of these extra Raman-active modes signifies that DW-driven lattice distortions induce a breaking of monoclinic $P2_1/c$ symmetry. Based on this we propose a third structural phase associated with the DW ordering in the pressure–temperature diagram of $\text{La}_4\text{Ni}_3\text{O}_{10}$, which is currently uncharted.

METHODS

Crystal growth

There are two methods to synthesize single crystals of $\text{La}_4\text{Ni}_3\text{O}_{10}$. One is using the floating zone technique with an image furnace under oxygen pressure [25] and the other one is by the flux method [56]. We used the latter technique resulting in flattened cuboid black crystals of $\text{La}_4\text{Ni}_3\text{O}_{10}$, with long edges of approximately 50-100 microns. La_2O_3 and Ni were ground together in stoichiometric ratio, then thoroughly mixed with K_2CO_3 flux in the molar ratio $\text{Ni}:\text{K}_2\text{CO}_3$ 1:35. The mixture was placed in an alumina crucible with a lid to prevent K_2CO_3 evaporation, then heated in a box furnace at 1050°C for 48 hours, cooled slowly to 975°C at 0.4°C/h, and cooled with the furnace inertia to room temperature.

The remaining flux was then washed away with distilled water. Powder X-ray diffraction data were collected with a Bruker D8-Endeavor with Cu $K\alpha$ radiation. The pattern of the pulverized reaction product shows $\text{La}_4\text{Ni}_3\text{O}_{10}$ as the majority phase, along with NiO and La_2NiO_4 as side products of the reaction.

Scanning Electron Microscope and Electron probe micro-analysis

Morphology of grains were investigated with a FESEM Zeiss Ultra+ scanning electron microscope. Energy dispersive X-ray analysis on selected crystals was carried out using a Bruker SDD detector and Spirit software. EPMA analysis were performed on a Jeol – 8800A electron microprobe equipped with five wavelength-dispersive spectrometers. Three of them were used to determine the chemical composition of grains: PETJ for Lanthanum ($\text{La}\alpha$), LiFH for Nickel ($\text{K}\alpha$), and LDE1H (W/Si) for oxygen ($\text{K}\alpha$). Analysis were made at 15 keV accelerating voltage, with a 30 nA probe current with 2 μm beam diameter. Similar conditions (counting times, current, samples and standards together in the chamber) were respected. KTiOPO_4 for Oxygen (40.4%, LaB_6 for Lanthanum and pure Nickel were used as standards. Concentrations were calculated using a $\Phi(\rho z)$ procedure. Both techniques confirm the La:Ni 4:3 atomic ratio.

Temperature dependent powder XRD

High temperature synchrotron powder XRD data were measured at BM01 (Swiss-Norwegian Beamlines, SNBL) at ESRF in Grenoble, France, at a wavelength of $\lambda = 0.71913$ Å and using a 2D PILATUS 2M detector [57]. The carefully ground powder sample was filled into a 0.1 mm diameter quartz capillary and heated with a resistive capillary heater [58]. Data were recorded every 2K from 290 to 1223 K in heating and cooling and Rietveld refinements were performed with the Fullprof software [59].

Temperature and Pressure dependent single crystal XRD

High-pressure experiments were performed at ID15b [60] ESRF Grenoble France, using membrane-driven diamond-anvil cells (DACs) with 500 μm diamond culets employing a

radiation of a wavelength of $\lambda = 0.4099 \text{ \AA}$. Diffracted intensity was collected on a EIGER 9M area detector during continuous rotation of the crystal about the ω axis, in frames of 0.5 deg rotation and 1 second exposure time. Stainless steel gasket were used for the pressure chambers. The pressure transmitting medium used was Helium, loaded at 1.2 kbar, to ensure high hydrostatic pressure conditions up to the highest pressure reached in this study. The pressure was measured using the R1-line emission of a ruby ball placed close to the sample using the International Practical Pressure Scale IPPS-Ruby2020 equation of state [61]. The ruby signal is measured before and after each measurement in order to control the pressure drift during acquisitions. The recorded pressure is set at the average of these two pressure values and the uncertainty is set as the half of the difference between these two values. It is typically found smaller than the symbol size used for the figures in this paper. The homogeneity of the pressure in the DAC was followed from both the width and the splitting between the R1 and R2 ruby lines [62, 63].

Under ambient pressure temperature-dependent single-crystal x-ray diffraction (SXRD) was measured at station EH1 of beamline P24 of PETRA-III extension at DESY in Hamburg, Germany, employing radiation of a wavelength of $\lambda = 0.5002 \text{ \AA}$. Diffracted X rays were detected by a Pilatus 1M CdTe detector. The temperature of the sample was regulated with a CRYOCOOL open-flow cryostat, employing helium as cryogenic gas. Crystal of 50 microns was selected for the SXRD experiment at beamline P24. Diffracted intensity was collected on the detector during continuous rotation of the crystal about the ϕ axis, in frames of 0.1 deg rotation and 0.1 second exposure time. Each run of data collection comprises a 10 times repeated measurement of 3600 frames, corresponding to a total rotation of the crystal by 360 deg, repeated 10 times. These data were binned to 360 frames of 1 deg of rotation and 10 seconds exposure time employing the software `addruncbf` and `combcbf` [64]. Due to the anisotropic shape of the reflection the EVAL15 suite [65] could not be used successfully. Instead, data processing has been done with the EVAL14 [66] was used to integrate the data. In EVAL14 the concept of ray tracing is not used, as EVAL14 defines a box, where inside box there is a reflection and outside the box no reflection. The border of the box is used for evaluating the background level. Integration now is simply adding up intensities of pixels inside the box. SADABS [67] has been used for the absorption correction for all the data sets. JANA2006 [68] was used for the structure refinements at 230 and 80 K.

Raman scattering

Raman measurements were performed with a 532 nm solid-state laser with an incident laser power between 0.5-2 mW. A Trivista 777 spectrometer equipped with ultra-low noise, cryogenically-cooled PyLon CCDs was used in single-stage configurations for which we have access to Raman signal down to 70 cm^{-1} . A cryo-free cryostat [69] was used to perform measurements down to 2 K (26 K with laser heating included).

Porto notation	$P2_1/c$	P_c	$P2_1$	$P\bar{1}$
X(YY) \bar{X}	24 A_g	51 A'	51 A	48 A_g
X(YZ) \bar{X}	24 B_g	51 A''	51 B	

TABLE I. The Raman observable symmetries for a given scattering orientation of light with respect to the global symmetry of the lattice of $\text{La}_4\text{Ni}_3\text{O}_{10}$. X,Y and Z are taken in the standard setting of the space group $P2_1/c$. The Poynting vector is perpendicular to X, while the polarization Y and Z are in the (bc) plane but not aligned with a particular axis. Y is defined to be perpendicular to Z. The second, third, fourth columns report the selection rules for the sub-groups of $P2_1/c$. P_c and $P2_1$ are consistent with the Raman results at low temperature while $P\bar{1}$ is not.

Ab initio density-functional theory calculation

The density-functional theory (DFT) crystal relaxation has been performed using the ABINIT code in the the PBE [47] generalized-gradient approximation (GGA) with pseudopotentials from the PsuedoDojo table. As explained in the main text, the calculation has been carried out in the lowest symmetry monoclinic $P2_1/c$ elementary and largest cell able to encompass all crystal structures up to the $I4/mmm$. Within this cell the total energy was found converged within 1 mHa using a plane-waves cutoff of 100 Ryd and a Brillouin zone k -point sampling of $2 \times 4 \times 4$ shifted by $1/2 \times 1/2 \times 1/2$ (as explained in the crystallographic part, within the $P2_1/c$ setting the Ruddlesden-Popper (RP) stacking axis is oriented along a and is doubled). The relaxation was stopped when the forces and stresses reduced below a threshold of only $5 \cdot 10^{-6} \text{ Ha/Bohr}$: this was an absolutely critical parameter of the

calculation to get the right phase diagram. With just only one order of magnitude more, $5 \cdot 10^{-5}$ Ha/Bohr, the relaxation could have stopped in the tetragonal (or even in one of the orthorhombic) at low pressure, when the minimum of the total energy was on the $P2_1/c$, and viceversa at highest pressure, depending on the starting crystal structure. It was not even a question of relative minima: just only tiny forces/stresses between energetically very close structures. Finally, the errors on lattice parameters have been estimated by calculating the stiffness tensor from the data out of the last four relaxation steps, and using its inverse, the compliance tensor, applied to the residual stress to evaluate the residual strain which is then taken as the lattice error estimate. We did the same to estimate the error on the octahedra tilt angle by relying on elastic constants associated to the internal atomic positions.

DATA AVAILABILITY

Data is available upon reasonable request from the authors.

ACKNOWLEDGMENTS

Beamtime for high pressure X-ray diffraction were performed in the beamline ID15b of the ESRF under the propoposal HC5916. For temperature-dependent X-ray diffraction measurements under ambient pressure, we acknowledge DESY (Hamburg, Germany), a member of the Helmholtz Association HGF, for the provision of experimental facilities. Beamtime was allocated for proposal R-20250763. We thank Martin Tolkiehn, Preeti Porkiyal and Heiko Schultz for their assistance with data collection at beamline P24 of PETRA-III at DESY. Computer time has been provided by GRICAD, project `mbqft`. S. R. and P. R. thank P. Monceau and J. E. Lorenzo for fruitful discussions. V. O. also thanks J. Even, C. Katan, A. Cano and Q. Meier for useful discussions on RP symmetries and their phase transitions. We thank the support from the Agence Nationale de la Recherche under the project SUPERNICKEL (Grant No.ANR-21-CE30-0041-04). M.-A.M. and Y. G. thank the European Research Council (ERC) under the European Union’s Horizon 2020 research and innovation program (Grant Agreement No. 865826).

AUTHOR CONTRIBUTIONS

E.P. and A.H.-A. synthesized the single crystals. V.O. carried out the DFT calculations. X-ray diffraction experiments were performed by S.R., E.P., G.G., O.P., A.P., D.V., D.C., L.N., C.P., S.vS., P.T. and P.R. EPMA was conducted by M.Q. and S.P. SXRD data analysis was carried out by S.R., while PXRD analysis was done by E.P. Raman measurements and analysis were done by Y.G. and M.A-M. The manuscript was written by S.R., Y.G., V.O., E.P., M.A-M. and P.R. with inputs from all authors. The project was initiated by P.T. and P.R. and the work was supervised by P.R.. Fundings were acquired by A.P., P.T., M.A-M. and P.R..

CORRESPONDING AUTHORS

Correspondence to Sitaram Ramakrishnan and Pierre Rodière.

ETHICS DECLARATION

Competing interests

The authors declare no competing interests.

-
- [1] Chu, C. W. and Hor, P. H. and Meng, R. L. and Gao, L. and Huang, Z. J. and Wang, and Y. Q., Evidence for superconductivity above 40 K in the La-Ba-Cu-O compound system, *Phys. Rev. Lett.* **58**, 405 (1987).
 - [2] H. Takagi, H. Eisaki, S. Uchida, A. Maeda, S. Tajima, K. Uchinokura and S. Tanaka, Transport and optical studies of single crystals of the 80-K Bi-Sr-Ca-Cu-O superconductor, *Nature* **332**, 236–238 (1988).
 - [3] B. Keimer, S. A. Kivelson, M. R. Norman, S. Uchida and J. Zaanen, From quantum matter to high-temperature superconductivity in copper oxides, *Nature* **518**, 179–186 (2015).
 - [4] J. M. Tranquada, D. J. Buttrey, V. Sachan, and J. E. Lorenzo, Simultaneous ordering of holes and spins in $\text{La}_2\text{NiO}_{4.125}$, *Phys. Rev. Lett.* **73**, 1003 (1994).

- [5] O. Zachar, S. A. Kivelson, and V. J. Emery, Landau theory of stripe phases in cuprates and nickelates, *Phys. Rev. B* **57**, 1422 (1998).
- [6] J. Zhang, Y.-S. Chen, D. Phelan, H. Zheng, M. R. Norman, and J. F. Mitchell, Stacked charge stripes in the quasi-2d trilayer nickelate $\text{La}_4\text{Ni}_3\text{O}_8$, *Proceedings of the National Academy of Sciences* **113**, 8945–8950 (2016).
- [7] B. Y. Wang, K. Lee, and B. H. Goodge, Experimental progress in superconducting nickelates, *Annual Review of Condensed Matter Physics* **15**, 305 (2024).
- [8] Y. Wang, K. Jiang, J. Ying, T. Wu, J. Cheng, J. Hu, and X. Chen, Recent progress in nickelate superconductors, *National Science Review* **12**, nwaf373 (2025).
- [9] D. Li, K. Lee, B. Y. Wang, M. Osada, S. Crossley, H. R. Lee, Y. Cui, Y. Hikita and Harold Y. Hwang, Superconductivity in an infinite-layer nickelate, *Nature* **572**, 624–627 (2019).
- [10] D. Li, B. Y. Wang, K. Lee, S. P. Harvey, M. Osada, B. H. Goodge, L. F. Kourkoutis, and H. Y. Hwang, Superconducting dome in $\text{Nd}_{1-x}\text{Sr}_x\text{NiO}_2$ infinite layer films, *Phys. Rev. Lett.* **125**, 027001 (2020).
- [11] S. Zeng, C. S. Tang, X. Yin, C. Li, M. Li, Z. Huang, J. Hu, W. Liu, G. J. Omar, H. Jani, Z. S. Lim, K. Han, D. Wan, P. Yang, S. J. Pennycook, A. T. S. Wee, and A. Ariando, Phase diagram and superconducting dome of infinite-layer $\text{Nd}_{1-x}\text{Sr}_x\text{NiO}_2$ thin films, *Phys. Rev. Lett.* **125**, 147003 (2020).
- [12] Y. E. Suyolcu, P. Puphal, and M. Hepting, Three generations of infinite-layer nickelate crystals, *MRS Communications* **15**, 169 (2025).
- [13] H. Sun, M. Huo, X. Hu, J. Li, Z. Liu, Y. Han, L. Tang, Z. Mao, P. Yang, B. Wang, J. Cheng, D. Yao, G.-M. Zhang and M. Wang, Signatures of superconductivity near 80 K in a nickelate under high pressure, *Nature* **621**, 493–498 (2023).
- [14] J. Hou, P.-T. Yang, Z.-Y. Liu, J.-Y. Li, P.-F. Shan, L. Ma, G. Wang, N.-N. Wang, H.-Z. Guo, J.-P. Sun, Y. Uwatoko, M. Wang, G.-M. Zhang, B.-S. Wang, and J.-G. Cheng, Emergence of high-temperature superconducting phase in pressurized $\text{La}_3\text{Ni}_2\text{O}_7$ crystals, *Chinese Physics Letters* **40**, 117302 (2023).
- [15] Y. Zhang, D. Su, Y. Huang, Z. Shan, H. Sun, M. Huo, K. Ye, J. Zhang, Z. Yang, Y. Xu, Y. Su, R. Li, M. Smidman, M. Wang, L. Jiao, and H. Yuan, High-temperature superconductivity with zero resistance and strange-metal behaviour in $\text{La}_3\text{Ni}_2\text{O}_{7-\delta}$, *Nature Physics* **20**, 1269 (2024).

- [16] G. Wang, N. Wang, T. Lu, S. Calder, J. Yan, L. Shi, J. Hou, L. Ma, L. Zhang, J. Sun, B. Wang, S. Meng, M. Liu, and J. Cheng, Chemical versus physical pressure effects on the structure transition of bilayer nickelates, *npj Quantum Materials* **10**, 1 (2025).
- [17] G. Wang, N. N. Wang, X. L. Shen, J. Hou, L. Ma, L. F. Shi, Z. A. Ren, Y. D. Gu, H. M. Ma, P. T. Yang, Z. Y. Liu, H. Z. Guo, J. P. Sun, G. M. Zhang, S. Calder, J.-Q. Yan, B. S. Wang, Y. Uwatoko, and J.-G. Cheng, Pressure-induced superconductivity in polycrystalline $\text{La}_3\text{Ni}_2\text{O}_{7-\delta}$, *Phys. Rev. X* **14**, 011040 (2024).
- [18] L. Wang, Y. Li, S.-Y. Xie, F. Liu, H. Sun, C. Huang, Y. Gao, T. Nakagawa, B. Fu, B. Dong, Z. Cao, R. Yu, S. I. Kawaguchi, H. Kadobayashi, M. Wang, C. Jin, H.-k. Mao, and H. Liu, Structure responsible for the superconducting state in $\text{La}_3\text{Ni}_2\text{O}_7$ at high-pressure and low-temperature conditions, *Journal of the American Chemical Society* **146**, 7506 (2024).
- [19] Y. Zhu, D. Peng, E. Zhang, B. Pan, X. Chen, L. Chen, H. Ren, F. Liu, Y. Hao, N. Li, Z. Xing, F. Lan, J. Han, J. Wang, D. Jia, H. Wo, Y. Gu, Y. Gu, L. Ji, W. Wang, H. Gou, Y. Shen, T. Ying, X. Chen, W. Yang, H. Cao, C. Zheng, Q. Zeng, J.-g. Guo, and J. Zhao, Superconductivity in pressurized trilayer $\text{La}_4\text{Ni}_3\text{O}_{10-\delta}$ single crystals, *Nature* **631** (2024).
- [20] M. Zhang, C. Pei, D. Peng, X. Du, W. Hu, Y. Cao, Q. Wang, J. Wu, Y. Li, H. Liu, C. Wen, J. Song, Y. Zhao, C. Li, W. Cao, S. Zhu, Q. Zhang, N. Yu, P. Cheng, L. Zhang, Z. Li, J. Zhao, Y. Chen, C. Jin, H. Guo, C. Wu, F. Yang, Q. Zeng, S. Yan, L. Yang, and Y. Qi, Superconductivity in trilayer nickelate $\text{La}_4\text{Ni}_3\text{O}_{10}$ under pressure, *Phys. Rev. X* **15**, 021005 (2025).
- [21] E. Zhang, D. Peng, Y. Zhu, L. Chen, B. Cui, X. Wang, W. Wang, Q. Zeng, and J. Zhao, Bulk superconductivity in pressurized trilayer nickelate $\text{Pr}_4\text{Ni}_3\text{O}_{10}$ single crystals, *Phys. Rev. X* **15**, 021008 (2025).
- [22] F. Li, Y. Hao, N. Guo, D. Jia, J. Dou, D. Peng, G. Zhang, L. Xiao, J. Zhang, W. Zhou, Y. Huang, X. Wang, Z. Guo, M. Mezouar, J. Elias F. S. Rodrigues, J. Luo, J. Yang, Q. Zeng, R. Zhou, H. Gou, Q. Zheng, G. Liu, and J. Zhang, Single-crystal structure determination of superconducting $\text{La}_4\text{Ni}_3\text{O}_{10-\delta}$ under high pressure, *Advanced Materials* **n/a**, e07365 (2025).
- [23] M. U. Nagell, W. A. Sławiński, P. Vajeeston, H. Fjellvåg, and A. O. Sjøstad, Temperature induced transitions in $\text{La}_4(\text{Co}_{1-x}\text{Ni}_x)_3\text{O}_{10+\delta}$; oxygen stoichiometry and mobility, *Solid State Ionics* **305**, 7 (2017).

- [24] J. Song, D. Ning, B. Boukamp, J.-M. Bassat, and H. J. M. Bouwmeester, Structure, electrical conductivity and oxygen transport properties of ruddlesden–popper phases $\text{Ln}_{n+1}\text{Ni}_n\text{O}_{3n+1}$ ($\text{Ln} = \text{La, Pr and Nd}$; $n = 1, 2 \text{ and } 3$), *J. Mater. Chem. A* **8**, 22206 (2020).
- [25] J. Zhang, D. Phelan, A. S. Botana, Y.-S. Chen, H. Zheng, M. Krogstad, S. G. Wang, Y. Qiu, J. A. Rodriguez-Rivera, R. Osborn, S. Rosenkranz, M. R. Norman, and J. F. Mitchell, Inter-twined density waves in a metallic nickelate, *Nature Communications* **11**, 6003 (2020).
- [26] S. Xu, C.-Q. Chen, M. Huo, D. Hu, H. Wang, Q. Wu, R. Li, D. Wu, M. Wang, D.-X. Yao, T. Dong, and N. Wang, Origin of the density wave instability in trilayer nickelate $\text{La}_4\text{Ni}_3\text{O}_{10}$ revealed by optical and ultrafast spectroscopy, *Phys. Rev. B* **111**, 075140 (2025).
- [27] M. Li, J. Gong, Y. Zhu, Z. Chen, J. Zhang, E. Zhang, Y. Li, R. Yin, S. Wang, J. Zhao, D.-L. Feng, Z. Du, and Y.-J. Yan, Direct visualization of an incommensurate unidirectional charge density wave in $\text{La}_4\text{Ni}_3\text{O}_{10}$, *Phys. Rev. B* **112**, 045132 (2025).
- [28] G. Wu, J. J. Neumeier, and M. F. Hundley, Magnetic susceptibility, heat capacity, and pressure dependence of the electrical resistivity of $\text{La}_3\text{Ni}_2\text{O}_7$ and $\text{La}_4\text{Ni}_3\text{O}_{10}$, *Phys. Rev. B* **63**, 245120 (2001).
- [29] H. Sakakibara, M. Ochi, H. Nagata, Y. Ueki, H. Sakurai, R. Matsumoto, K. Terashima, K. Hirose, H. Ohta, M. Kato, Y. Takano, and K. Kuroki, Theoretical analysis on the possibility of superconductivity in the trilayer ruddlesden–popper nickelate $\text{La}_4\text{Ni}_3\text{O}_{10}$ under pressure and its experimental examination: Comparison with $\text{La}_3\text{Ni}_2\text{O}_7$, *Phys. Rev. B* **109**, 144511 (2024).
- [30] J. Huang and T. Zhou, Interlayer pairing-induced partially gapped fermi surface in trilayer $\text{La}_4\text{Ni}_3\text{O}_{10}$ superconductors, *Phys. Rev. B* **110**, L060506 (2024).
- [31] Z. Ouyang, R.-Q. He, and Z.-Y. Lu, Phase diagrams and two key factors to superconductivity of ruddlesden–popper nickelates, *Phys. Rev. B* **112**, 045127 (2025).
- [32] C.-Q. Chen, Z. Luo, M. Wang, W. Wú, and D.-X. Yao, Trilayer multiorbital models of $\text{La}_4\text{Ni}_3\text{O}_{10}$, *Phys. Rev. B* **110**, 014503 (2024).
- [33] Y. Zhang, L.-F. Lin, A. Moreo, T. A. Maier, and E. Dagotto, Prediction of s^\pm -wave superconductivity enhanced by electronic doping in trilayer nickelates $\text{La}_4\text{Ni}_3\text{O}_{10}$ under pressure, *Phys. Rev. Lett.* **133**, 136001 (2024).
- [34] M. Zhang, H. Sun, Y.-B. Liu, Q. Liu, W.-Q. Chen, and F. Yang, Spin-density wave and superconductivity in $\text{La}_4\text{Ni}_3\text{O}_{10}$ under ambient pressure, *Phys. Rev. B* **111**, 144502 (2025).

- [35] S. Xu, H. Wang, M. Huo, D. Hu, Q. Wu, L. Yue, D. Wu, M. Wang, T. Dong, and N. Wang, Collapse of density wave and emergence of superconductivity in pressurized-La₄Ni₃O₁₀ evidenced by ultrafast spectroscopy, *Nature Communications* **16**, 7039 (2025).
- [36] S. Kumar, Øystein Fjellvåg, A. O. Sjøstad, and H. Fjellvåg, Physical properties of ruddlesdenpopper (n=3) nickelate: La₄Ni₃O₁₀, *Journal of Magnetism and Magnetic Materials* **496**, 165915 (2020).
- [37] J. Zhang, H. Zheng, Y.-S. Chen, Y. Ren, M. Yonemura, A. Huq, and J. F. Mitchell, High oxygen pressure floating zone growth and crystal structure of the metallic nickelates $R_4\text{Ni}_3\text{O}_{10}$ ($r = \text{La, Pr}$), *Phys. Rev. Mater.* **4**, 083402 (2020).
- [38] D. Rout, S. R. Mudi, M. Hoffmann, S. Spachmann, R. Klingeler, and S. Singh, Structural and physical properties of trilayer nickelates $R_4\text{Ni}_3\text{O}_{10}$ ($r = \text{La, pr, and nd}$), *Phys. Rev. B* **102**, 195144 (2020).
- [39] See Supplemental Material at [URL will be inserted by publisher] for details on the diffraction, Raman experiments and values of the structural parameters.
- [40] S. van Smaalen, *Incommensurate Crystallography*, International Union of Crystallography Monographs on Crystallography (OUP Oxford, 2007).
- [41] S. Parsons, Introduction to twinning, *Acta Crystallographica Section D* **59**, 1995 (2003).
- [42] S. Ramakrishnan, S. R. Kotla, H. Pi, B. B. Maity, J. Chen, J.-K. Bao, Z. Guo, M. Kado, H. Agarwal, C. Eisele, M. Nohara, L. Noohinejad, H. Weng, S. Ramakrishnan, A. Thamizhavel, and S. van Smaalen, Noncentrosymmetric, transverse structural modulation in SrAl_4 , and elucidation of its origin in the BaAl_4 family of compounds, *Phys. Rev. Res.* **6**, 023277 (2024).
- [43] S. R. Kotla, S. Ramakrishnan, A. M. Schaller, T. Rekis, C. Eisele, J.-K. Bao, L. Noohinejad, G. de Laitre, M. de Boissieu, and S. van Smaalen, Deciphering the commensurately modulated monoclinic phase of Rb_2ZnCl_4 at low temperatures, *Journal of Solid State Chemistry* **345**, 125226 (2025).
- [44] G. Chapuis, F. Hulliger, and R. Schmelczer, The crystal structure and some properties of Eu_2Sb_3 , *Journal of Solid State Chemistry* **31**, 59 (1980).
- [45] M. B. Shoker, S. Ramakrishnan, B. Croes, O. Cregut, N. Beyer, K. Dorkenoo, P. Rodière, B. Wehinger, G. Garbarino, M. Mezouar, M. Verseils, P. Fertey, S. Cherifi-Hertel, P. Bouvier, and M. Guennou, An underdog story: Re-emergence of a polar instability at high pressure in

- knbo3 (2025), arXiv:2508.06399 [cond-mat.mtrl-sci].
- [46] S. Nandi, B. Maity, S. Dan, K. Ali, B. Patra, A. Mondal, G. Garbarino, P. Rodière, S. Ramakrishnan, B. Singh, and A. Thamizhavel, Evidence of electronic instability driven structural distortion in the nodal line semimetal cosn_2 (2025), arXiv:2509.23221 [cond-mat.mtrl-sci].
 - [47] J. P. Perdew, K. Burke, and M. Ernzerhof, Generalized gradient approximation made simple, *Phys. Rev. Lett.* **77**, 3865 (1996).
 - [48] D.-H. Gim, C. H. Park, and K. H. Kim, Orbital-selective quasiparticle depletion across the density wave transition in trilayer nickelate $\text{La}_4\text{Ni}_3\text{O}_{10}$, *Physical Review Letters* **135**, 136505 (2025).
 - [49] A. Suthar, V. Sundaramurthy, M. Bejas, C. Le, P. Puphal, P. Sosa-Lizama, A. Schulz, J. Nuss, M. Isobe, P. A. van Aken, *et al.*, Multiorbital character of the density wave instability in $\text{La}_{4-x}\text{Ni}_3\text{O}_{10}$, arXiv preprint arXiv:2508.06440 (2025).
 - [50] S. Deswal, D. Kumar, D. Rout, S. Singh, and P. Kumar, Dynamics of electron–electron correlation and electron–phonon coupled phase progression in trilayer nickelate $\text{La}_4\text{Ni}_3\text{O}_{10}$, *Applied Physics Letters* **127** (2025).
 - [51] W. J. Schutte, F. Disselborg, and J. L. de Boer, Determination of the two-dimensional incommensurately modulated structure of Mo_2S_3 , *Acta Crystallogr. B* **49**, 787 (1993).
 - [52] S. Ramakrishnan, A. Schönleber, C. B. Hübschle, C. Eisele, A. M. Schaller, T. Rekiş, N. H. A. Bui, F. Feulner, S. van Smaalen, B. Bag, S. Ramakrishnan, M. Tolkehn, and C. Paulmann, Charge density wave and lock-in transitions of CuV_2S_4 , *Phys. Rev. B* **99**, 195140 (2019).
 - [53] S. Ramakrishnan, S. R. Kotla, T. Rekiş, J.-K. Bao, C. Eisele, L. Noohinejad, M. Tolkehn, C. Paulmann, B. Singh, R. Verma, B. Bag, R. Kulkarni, A. Thamizhavel, B. Singh, S. Ramakrishnan, and S. van Smaalen, Orthorhombic charge density wave on the tetragonal lattice of EuAl_4 , *IUCrJ* **9**, 378 (2022).
 - [54] D. E. Bugaris, C. D. Malliakas, F. Han, N. P. Calta, M. Sturza, M. J. Krogstad, R. Osborn, S. Rosenkranz, J. P. C. Ruff, G. Trimarchi, S. L. Bud’ko, M. Balasubramanian, D. Y. Chung, and M. G. Kanatzidis, Charge density wave in the new polymorphs of $\text{RE}_2\text{Ru}_3\text{Ge}_5$ (RE= Pr, Sm, Dy), *Journal of the American Chemical Society* **139**, 4130 (2017).
 - [55] V. Sharma, S. Ramakrishnan, J. SS, S. R. Kotla, B. Maiti, C. Eisele, H. Agarwal, L. Noohinejad, M. Tolkehn, D. Bansal, S. van Smaalen, and T. Arumugam, Room temperature charge density wave in a tetragonal polymorph of $\text{Gd}_2\text{O}_3\text{Si}_5$ and study of its origin in the $\text{Re}_2\text{T}_3\text{X}_5$ (re

- = rare earth, t = transition metal, x = si, ge) series, Chemistry of Materials **36**, 6888 (2024).
- [56] F. Li, S. Wang, C. Ma, X. Wang, C. Liu, C. Fan, L. Han, S. Wang, X. Tao, and J. Zhang, Flux growth of trilayer $\text{La}_4\text{Ni}_3\text{O}_{10}$ single crystals at ambient pressure, Crystal Growth & Design **24**, 347 (2024).
- [57] V. Dyadkin, P. Pattison, V. Dmitriev, and D. Chernyshov, A new multipurpose diffractometer PILATUS@SNBL, Journal of Synchrotron Radiation **23**, 825 (2016).
- [58] K. P. Marshall, H. Emerich, C. J. McMonagle, C. A. Fuller, V. Dyadkin, D. Chernyshov, and W. van Beek, A new high temperature, high heating rate, low axial gradient capillary heater, Journal of Synchrotron Radiation **30**, 267 (2023).
- [59] J. Rodríguez-Carvajal, Recent advances in magnetic structure determination by neutron powder diffraction, Physica B: Condensed Matter **192**, 55 (1993).
- [60] G. Garbarino, M. E. Hanfland, S. Gallego-Parra, A. D. Rosa, M. Mezouar, D. Duran, K. Martel, E. Papillon, T. Roth, P. Got, and J. Jacobs, Extreme conditions X-ray diffraction and imaging beamline ID15B on the ESRF extremely brilliant source, High Press. Res. **44**, 199 (2024).
- [61] G. Shen, Y. Wang, A. Dewaele, C. Wu, D. E. Fratanduono, J. Eggert, S. Klotz, K. F. Dziubek, P. Loubeyre, O. V. Fat'yanov, P. D. Asimow, T. Mashimo, and R. M. M. Wentzcovitch, Toward an international practical pressure scale: A proposal for an ipps ruby gauge (ipps-ruby2020), High Pressure Research **40**, 299 (2020).
- [62] K. Takemura, Evaluation of the hydrostaticity of a helium-pressure medium with powder x-ray diffraction techniques, Journal of Applied Physics **89**, 662 (2001).
- [63] A. Dewaele and P. Loubeyre, Pressurizing conditions in helium-pressure-transmitting medium, High Pressure Research **27**, 419 (2007).
- [64] C. Paulmann, *P24ToolsCP, v1.12, software tools for postprocessing area detector, x-ray diffraction data* (2022).
- [65] A. M. M. Schreurs, X. Xian, and L. M. J. Kroon-Batenburg, EVAL15: a diffraction data integration method based on ab initio predicted profiles, J. Appl. Crystallogr. **43**, 70 (2010).
- [66] A. J. M. Duisenberg, L. M. J. Kroon-Batenburg, and A. M. M. Schreurs, An intensity evaluation method: EVAL-14, Journal of Applied Crystallography **36**, 220 (2003).
- [67] G. M. Sheldrick, *SADABS, Version 2008/1* (Göttingen: University of Göttingen, 2008).

- [68] V. Petricek, M. Dusek, and L. Palatinus, Crystallographic computing system JANA2006: general features, *Z. Kristallogr.* **229**, 345 (2014).
- [69] M. Zeman, B. Lefevre, S. Dang, T. Trolhier, P. Camus, and T. Chaneière, Design and performances of a dry table-top optical cryostat at 2k, *IOP Conference Series: Materials Science and Engineering* **1327**, 012153 (2025).